UC Berkeley
SEMM Reports Series

Title

Simulation of dynamic shear band propagation. Part I: Failure mode transition

Permalink

https://escholarship.org/uc/item/4nn892pm

Authors

Li, Shaofan
Liu, Wing-Kam
Rosakis, Ares
et al.

Publication Date

2000-08-01

STRUCTURAL ENGINEERING
MECHANICS AND MATERIALS

SIMULATION OF DYNAMIC SHEAR BAND PROPAGATION. PART I: FAILURE MODE TRANSITION

BY

SHAOFAN LI
WING-KAM LIU
ARES J. ROSAKIS
WEI HAN
AND
TED BELYTSCHKO

Simulations of Dynamic Shear Band Propagation
Part I : Failure Mode Transition

Shaofan Li [1] and Wing-Kam Liu[†][2] and Ares J. Rosakis[‡][3]
and Wei Hao[†][4] and Ted Belytschko[†][5]

Department of Civil and Environmental Engineering,
University of California, Berkeley, CA 94720 U.S.A.
†Department of Mechanical Engineering, Northwestern University,
2145 Sheridan Road, Evanston, IL 60208 U.S.A. ;
‡Graduate Aeronautical Laboratories, California Institute of Technology,
Pasadena, CA 91125 U.S.A.

Abstract

A meshfree approximation is used for both three-dimensional (3D) and two-dimensional (2D) numerical simulations of dynamic shear band propagation in an impact-loaded prenotched plate. The experiment for this type of problems was initially proposed and studied by Kalthoff and Winkler [1987] (the Kalthoff-Winkler problem), and later the experiment was re-designed, refined, and re-examined by Zhou, Rosakis and Ravichandran [1996] (the Zhou-Rosakis-Ravichandran problem) and others.

The main contributions of this numerical study are twofolds. First, failure mode transition and failure mode switching have been observed in numerical computations. In the intermediate impact velocity range ($20m/s < V < 30m/s$), the numerical results here ($V = 25m/s$) show that there is a failure mode switch (ductile-to-brittle) phenomenon, i.e. a cleavage crack initiates from the tip of the dynamic shear band. In the high impact velocity range ($V > 30m/s$), the numerical results ($V = 33m/s$ & $V = 37m/s$) show that the dynamic shear band penetrates through the specimen without cleavage type fracture, which is a typical ductile failure mode. That is, as impact velocity increases, the failure mode of the impact-loaded plate changes following the direction from brittle-to-ductile. Second, the results of this simulation show in the first time that there is indeed an autonomous, self-similar, high strain rate region in front of the shear band tip, which, we believe, is the driven force for the formation and propagation of a dynamic adiabatic shear band. In addition, the curved shear band formation observed in experiment is also accurately captured in the meshfree simulation.

Key Words: *Adiabatic Shear Band, Dynamic Shear Band Propagation, Crack Propagation, Failure Mode Transition, Meshfree Methods, Strain Localization, Curved Shear Band, Multi-physics modeling*

1 Introduction

In 1987, Kalthoff and Winkler presented and later published their experimental results on a pre-notched plate subjected high speed impact[9]. In that experiment, a thin metal plate with two pre-notches is used as the target specimen, and a cylinder projectile with flat end, after being accelerated by an air gun to speeds ranging from $10m/s$ to $100m/s$, impacts the specimen in the region between the two cracks (see Fig. 1). The impact initiates a compression wave in the plate, which generates a mode-II dynamic loading at the crack tip, and it then produces high temperature rise inside the plate, which subsequently leads to either fracture, or material instability at the tip of the pre-notch. There are two major concerns: (1) under which conditions, cleavage fracture occurs (brittle failure), and under which conditions, material instability occurs (ductile failure); (2) if material instability occurs, can it propagate as dynamic shear band propagation.

It was found ([9]) that when the impact velocity exceeds certain limit V_{TF} a crack is initiated from the notch tip and propagates in a direction that forms a 70° angle with the notch line direction (1). This cleavage type of brittle failure is somewhat expected based on conventional fracture theory. What was unexpected is that when the impact velocity exceeds another (higher) threshold V_{SB}, the failure mode changes: a shear band is initiated at the notch tip and propagates through the specimen, which is a purely ductile failure phenomenon. This change of failure modes with increase of impact speed has been referred to as failure mode transition.

The experiment has revealed something fundamentally different from conventional thinking. First under extremely high strain rate shear loading, the material failure seems to be dominated by ductile failure. Second, the failure mode transition follows the direction of brittle-to-ductile as impact velocity increases, which is in contrast to the traditional belief, in which it had been speculated that the material failure mechanism follows the opposite direction i.e. ductile-to-brittle, as strain rate increases. The double notch impact plate

[1] corresponding author, li@ce.berkeley.edu

[2] w-liu@nwu.edu

[3] rosakis@aero.caltech.edu

[4] haowei@nwu.edu
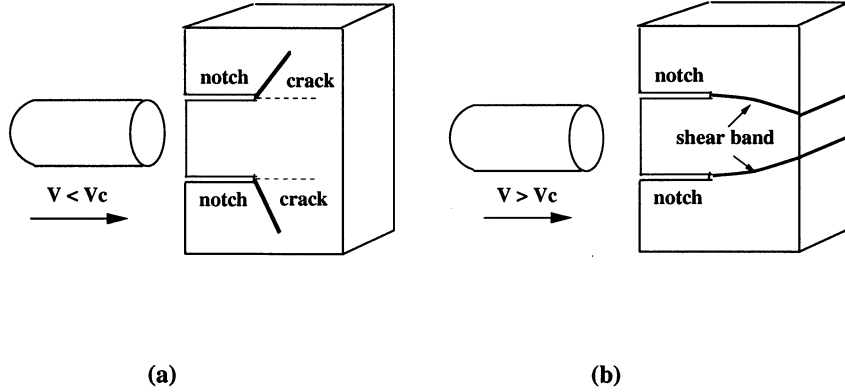
[5] t-belytschko@nwu.edu

2

Fig. 1. The Kalthoff-Winkler problem

experiment, i.e. the Kalthoff-Winkler problem suffers the setback of stress wave interaction due to two different pre-cracks, and complicates experimental conditions. To improve the accuracy of the experiment, Rosakis and his co-workers at California Institute of Technology(Mason, Rosakis, and Ravichandran [21], and later Zhou, Rosakis, and Ravichandran [34]) have systematically studied the problem; they carefully re-designed the experiment, and used a single notch plate of a maraging steel C-300 and Ti-6Al-4V alloy as the target specimen, which is referred to as the Zhou-Rosakis-Ravichandran problem. The main advantage of using a single notch specimen is that it eliminates the interference of the diffraction wave between notches, which had occurred in Kalthoff's original experiment, so that a longer loading can be achieved at the notch tip, which may help to intensity the physical phenomenon, and isolate various different factors in the process. By doing so, they found an unusaul mode switching phenomenon. In the intermediate range impact velocity $(20m/s < V < 29.6m/s)$, different from Kalthoff's results, at first a shear band initiates from the notch tip, propagates, and is arrested, then suddenly a cleavage type crack initiates from the arrested shear band tip. This is a failure mode transition, or switch at a fixed impact velocity; more precisely speaking, it is a failure mode switch from ductile failure (shear band propagation) to brittle failure (cleavage fracture). Again, at higher impact velocities $(V > 29.6m/s)$, they confirmed Kalthoff's result, i.e. the shear band propagates and penetrates through the specimen without cleavage fracture, which indicates the dominance of the ductile failure at high strain rate (see Fig. 2).

Simulating Kalthoff-Winkler problem, or Zhou-Rosakis-Ravichandran problem in numerical computations is, nonetheless, less satisfactory. The challenge here is how to realize the failure mode transition in numerical computation. The first numerical simulation related to the high speed bullet/plate impact problem was conducted by Needleman and Tvergaard [26]. To explain the unusual brittle-to-ductile mode transition observed in experiments, they attributed the factor to the fact that high strain rate loading enhances thermal softening, which in turn suppresses the build-up of the maximum hoop stress, and thus the system is more prone to the ductile failure than brittle failure, i.e.,

3

<div align="center">(a)</div>
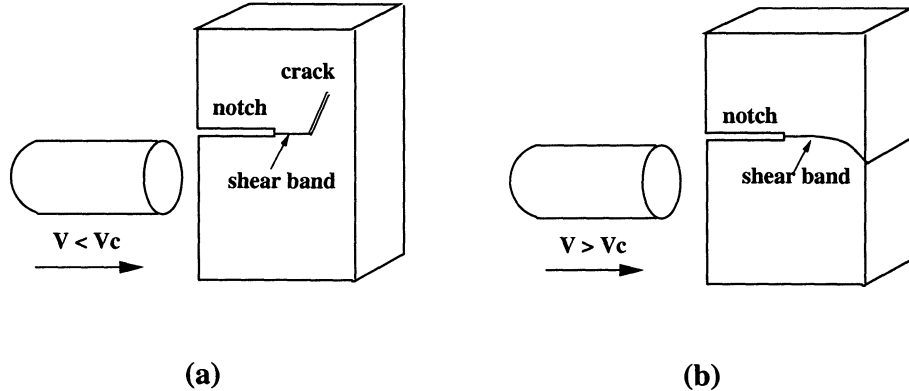
<div align="center">(b)</div>

Fig. 2. The Zhou-Rosakis-Ravichandran problem

the dynamic shear band propagation prevails over cleavage crack propagation. Zhou, Ravichandran, and Rosakis [33] simulated the experiment numerically, and introduced a viscous fluid-type of constitutive equation, to mimic the drastic reduction of shear force carrying capability of shear band. However, both numerical experiments had not been able to accurately predict to the failure mode switch/transition. On the other hand, in both finite element computations [26,33], mesh-dependence effects are reported. The work, [33], is the only successful simulation so far on dynamic shear band propagation; a shear band computed is a straight line along the finite element boundary, parallel to initial pre-notch line. A meshfree simulation was conducted by Belytchko and Tabbara [2] using the element-free Galerkin method to simulate the double notch specimen impact by assuming that it is an elastodynamic process. Recently, Klein [10] again used the element free Galerkin (EFG) method to simulate the Kalthoff problem (the double notch specimen), with a hyper-elastic based cohesive model — the internal virtual bond (IVB) constitutive model [5]. Both numerical computations found that a crack initiates from the notch tip at about a 70° angle as observed in the Kalthoff's original experiment. Again, the above mentioned numerical computations could not simulate the failure mode switch/transition, nor dynamic shear band propagation. Furthermore, most of the numerical computations conducted so far are two-dimensional, and some of the important aspects of the physical phenomenon of the problem have not been predicted, or identified accurately in numerical simulations, such as failure mode transition/switch, shear band configuration/structure.

The objective of this work is aimed at a comprehensive numerical simulation of the Zhou-Rosakis-Ravichandran problem (single notch problem). It is aimed at providing an accurate numerical simulation in major aspects of the physical process, which should includes failure mode transition, failure mode switch, shear band propagation and configuration, local/global temperature distribution field, stress distribution, inelastic strain/strain rate distribution, as well as three-dimensional effects.

From computational standpoint, the meshfree method has been proven to be

<div align="center">4</div>

superior than conventional finite element methods in numerical simulation of shear band formation (see: Li & Liu [15], and Li, Hao, and Liu [13]). It is less prone to the mesh alignment sensitivity, and it has the ability to relief volumetric locking in displacement based formulation (the advantage in 3-D simulation is obvious), and in turn, it is easy to implement in explicit computations, which is very suitable in dynamic simulations.

The arrangement of the paper is as follows: meshfree methods, in particular, the Reproducing Kernel Particle Method (RKPM) [18,17,19] is reviewed in Section 2, together, an explicit meshfree Galerkin formulation is outlined. In this simulation, a thermo-elasto-viscoplastic constitutive model is adopted, which is the same as used by Zhou et al. [33,35], except here only adiabatic heating is considered. By doing so, the Pierce's rate tangent modulus method [27] is extended to include the adiabatic heating, which are discussed in Section 3. In Section 4, numerical results are presented and discussed.

2   An explicit meshfree Galerkin formulation

There are several meshfree methods currently used in computational mechanics, such as smoothed particle hydrodynamics (SPH) [23], diffuse element method (DEM) [24], element-free Galerkin (EFG) [1], reproducing kernel particle method (RKPM) [18,16,20], etc. . The particular meshfree method used in this simulation is the reproducing kernel particle method (RKPM). A detailed account of the method can be found in Liu, Li, and Belytschko [19] and Li & Liu [14].

The basic idea of reproducing kernel particle method (RKPM) is to construct a proper kernel function such that one can approximate the function of interest through a "reproducing" or "filtering" representation

$$u_\varrho(x) = \mathcal{R}_\varrho u(x) = \int_\Omega \mathcal{K}_\varrho(y - x)u(y)d\Omega \qquad (1)$$

where $\mathcal{K}_\varrho(X) := 1/\varrho^n \mathcal{K}(X/\varrho)$, ρ is the dilation parameter that is associated with the support size of the kernel function, and n is spatial dimension. The RKPM kernel function is compact supported, and usually very smooth, $\mathcal{K}(X) \in C^N(\Omega)$ and $N >> 1$. Note that a RKPM representation is a spatial convolution in a strict sense, whereas the finite element interpolation can be viewed as a spatial convolution only in the sense that the kernel function is a generalized function. Assume that in the domain Ω there is a valid particle distribution, $\Lambda := \{1, 2, \cdots, \cdots, NP\}$. Discretizing (1) yields a discrete

5

convolution, which is defined as

$$u^h(X) = (\mathcal{K}_\varrho *' u)(X) := \sum_{I=\Lambda} \mathcal{K}_\varrho(X_I - X)\Delta V_I u_I \qquad (2)$$

For simplicity, in the rest of the paper, we shall simply denote $\mathcal{K}_\varrho(X_I - X)\Delta V_I$ as $\mathcal{K}_I(X)$. Eq. (2) can be viewed as a nonlocal interpolation (or not a "interpolation" based on conventional definition). In such "nonlocal interpolation", any point in the domain, including particle point, is covered by multiple shape functions.

We begin with defining and describing the kinematic quantities at finite strains. Followed the standard convention that $\mathbf{x}$ denotes the spatial coordinate of a material point and $\mathbf{X}$ denotes the referential coordinate of that material point, the displacement of the material point is defined as

$$\mathbf{u} := \mathbf{x} - \mathbf{X} \qquad (3)$$

The deformation gradient and velocity field are given by

$$\mathbf{F} := \frac{\partial \mathbf{x}}{\partial \mathbf{X}} \qquad (4)$$

A weak form of the balance of linear momentum can be written as

$$\int_{\Omega_0} \mathbf{P} : \delta \mathbf{F}^T d\Omega = \int_{\Omega_0} \rho_0 \mathbf{B} \cdot \delta \mathbf{u} d\Omega + \int_{\Gamma^{trac}} \mathbf{T} \cdot \delta \mathbf{u} dS - \int_{\Omega_0} \rho_0 \frac{\partial^2 \mathbf{u}}{\partial t^2} \delta \mathbf{u} d\Omega \qquad (5)$$

where $\mathbf{T}$ is the prescribed traction on the traction boundary, Γ^{trac}, and $\mathbf{P}$ denotes the first Piola-Kirchhoff stress tensor, which can be related to the Kirchhoff stress tensor as $\boldsymbol{\tau} = \mathbf{F} \cdot \mathbf{P}$. For simplicity, the boundary conditions are specified with respect to the referential configuration,

$$\mathbf{n}_0 \mathbf{P} = \mathbf{T}^0 \,, \quad \forall \, \mathbf{X} \in \Gamma_X^T \qquad (6)$$
$$\mathbf{u} = \mathbf{u}^0 \,, \quad \forall \, \mathbf{X} \in \Gamma_X^u \qquad (7)$$

where $\Gamma_X^T \cup \Gamma_X^u = \partial \Omega_X$.

It should be noted that unlike FE approximation, the RKPM interpolant has a shortcoming: that is its inability to represent essential boundary condition via boundary value interpolation. Therefore, there is an extra term missing in

the weak form (5)

$$\int_{\Gamma^u_X} \mathbf{T}\delta\mathbf{u}d\Gamma \tag{8}$$

because $\delta\mathbf{u} \neq 0$, $\forall \ X \in \Gamma^u_X$. On how to account and estimate this term and enforce the essential conditions, readers may refer to [15].

Assume that the trial, and weighting functions have the forms

$$\mathbf{u}^h(X,t) = \sum_{I=1}^{NP} N_I(X)\mathbf{d}_I(t) \tag{9}$$

$$\delta\mathbf{u}^h(X,t) = \sum_{I=1}^{NP} N_I(X)\delta\mathbf{d}_I(t) \tag{10}$$

The weak form (5) will yield the following discrete equations

$$\mathbf{M}\frac{\partial^2\mathbf{u}^h}{\partial t^2} = \mathbf{f}^{ext} - \mathbf{f}^{int} \tag{11}$$

The conventional row-sum lumped mass is adopted in the computation, and the external and internal forces are calculated as follows,

$$\mathbf{f}_I^{ext} = \int_{\Gamma^{trac}} T_i(X,t)N_I\mathbf{e}_i dS + \int_{\Omega_0} \rho_0 B_i(X,t)N_I(X)\mathbf{e}_i d\Omega \tag{12}$$

$$\mathbf{f}_I^{int} = \int_{\Omega_0} P_{Ji}^h \frac{\partial N_I}{\partial X_J}\mathbf{e}_i d\Omega \ . \tag{13}$$

where $\mathbf{e}_i, i = 1, 2, 3$ are the unit vector of referential coordinate.

3 Constitutive modelings

In inelastic large deformation, the deformation gradient, $\mathbf{F}$, can be decomposed as

$$\mathbf{F} = \mathbf{F}^e \cdot \mathbf{F}^{vp} \tag{14}$$

where $\mathbf{F}^e$ describes elastic deformation and rigid body rotation and $\mathbf{F}^{vp}$ represents viscous inelastic deformation. The rate of deformation tensor, $\mathbf{D}$, and

7

the spin tensor, $\mathbf{W}$, are the symmetric part and anti-symmetric part of spatial velocity gradient $\mathbf{L} = \dot{\mathbf{F}} \cdot \mathbf{F}^{-1}$, i.e.

$$\mathbf{D} + \mathbf{W} = \dot{\mathbf{F}} \cdot \mathbf{F}^{-1} = \dot{\mathbf{F}}^{\mathbf{e}} \cdot \mathbf{F}^{\mathbf{e}-1} + \mathbf{F}^{\mathbf{e}} \cdot \dot{\mathbf{F}}^{\mathbf{vp}} \cdot \mathbf{F}^{\mathbf{vp}-1} \cdot \mathbf{F}^{\mathbf{e}-1} \qquad (15)$$

by using the fact that $\dot{\mathbf{F}} = \dot{\mathbf{F}}^e \mathbf{F}^{vp} + \mathbf{F}^e \dot{\mathbf{F}}^{vp}$ and $\mathbf{F}^{-1} = \mathbf{F}^{vp-1} \mathbf{F}^{e-1}$. Consequently, the following decomposition holds

$$\mathbf{D}^e + \mathbf{D}^T + \mathbf{W}^\mathbf{e} = \dot{\mathbf{F}}^e \cdot \mathbf{F}^{\mathbf{e}-1} \qquad (16)$$

$$\mathbf{D}^{vp} + \mathbf{W}^\mathbf{P} = \mathbf{F}^e \cdot \dot{\mathbf{F}}^{vp} \cdot \mathbf{F}^{vp-1} \cdot \mathbf{F}^{\mathbf{e}-1} \qquad (17)$$

Note that thermal deformation is always dilatational, and $\mathbf{W}^\mathbf{T} = \mathbf{0}$.

The general balance of energy rate is formulated in current configuration:

$$\int_\Omega \rho \dot{e} d\Omega + \frac{d}{dt} \int_\Omega \frac{1}{2}\rho \dot{\mathbf{u}} \cdot \dot{\mathbf{u}} d\Omega = \int_{\partial\Omega} \mathbf{t} \cdot \mathbf{v} dS - \int_{\partial\Omega} \bar{q} dS \qquad (18)$$

where e is the density of internal energy; $\mathbf{t}$ is the flux of mechanical force, or traction; and $\bar{q}$ is the heat flux through the boundary.

Considering the rate form of principle of virtual work, we have

$$\int_{\partial\Omega} \mathbf{t} \cdot \mathbf{v} d\Omega = \int_\Omega \boldsymbol{\sigma} : \mathbf{D} d\Omega + \frac{d}{dt} \int_\Omega \frac{1}{2}\rho \dot{\mathbf{u}} \cdot \dot{\mathbf{u}} d\Omega \qquad (19)$$

And pull-back the rate conservation form into the referential configuration yields

$$\int_{\Omega_0} \rho_0 \dot{e} d\Omega = \int_{\Omega_0} \boldsymbol{\tau} : \mathbf{D} d\Omega - \int_{\partial\Omega_0} J\hat{\mathbf{N}} \cdot \mathbf{F}^{-1} \cdot \bar{q} dS \qquad (20)$$

in which, the standard volume/area transformations, $d\Omega = Jd\Omega_0$, $J = det\{\mathbf{F}\}$, $\hat{n}dS = J\hat{\mathbf{N}}\mathbf{F}^{-1}dS_0$, are used, where $\hat{n}$ and $\hat{\mathbf{N}}$ are the normal of surface element for spatrial configuration and referential configuration respectively.

Suppose that the heat flux is driven by temperature gradient. Then

$$\bar{q} = -\boldsymbol{\kappa} \cdot \frac{\partial T}{\partial \mathbf{x}} = -\boldsymbol{\kappa} \cdot \frac{\partial T}{\partial \mathbf{X}} \cdot \frac{\partial \mathbf{X}}{\partial \mathbf{x}} = -\boldsymbol{\kappa} \cdot \frac{\partial T}{\partial \mathbf{X}} \cdot \mathbf{F}^{-1} = -\boldsymbol{\kappa} \cdot \mathbf{F}^{-T} \cdot \frac{\partial T}{\partial \mathbf{X}} \quad (21)$$

where $\boldsymbol{\kappa}$ is the heat capacitance tensor.

8

Neglecting thermo-elastic coupling, i.e. $\boldsymbol{\tau} : \mathbf{D}^e \approx 0$, we postulate that a major part of plastic work will convert into heat (Taylor & Quinney [29]). and using the specific heat at constant pressure to approximate the specific heat at constant stress, one can obtain the following balance form via Gauss's theorem

$$\int\limits_V \rho_0 C_p \dot{T} d\Omega = \int\limits_V \chi \boldsymbol{\tau} : \mathbf{D}^{vp} d\Omega + \int\limits_V \nabla_{\mathbf{X}} (J \cdot \mathbf{F}^{-1} \cdot \boldsymbol{\kappa} \cdot \mathbf{F}^{-T} \cdot \nabla_{\mathbf{X}} T) d\Omega \quad (22)$$

where $V \subset \Omega_0$, is any subset of Ω_0. Thus it yields the following strong form

$$\rho_0 C_p \frac{\partial T}{\partial t} = \chi \boldsymbol{\tau} : \mathbf{D}^{vp} + \nabla_{\mathbf{X}} \Big(J \mathbf{F}^{-1} \cdot \boldsymbol{\kappa} \cdot \mathbf{F}^{-T} \cdot \nabla_{\mathbf{X}} T \Big), \quad \forall \mathbf{X} \in \Omega_0 \quad (23)$$

Because the whole impact process occurs within 300 μs, the effect of heat conduction should be a higher order factor. Considering adiabatic heating, i.e. neglecting heat conduction, we have

$$\rho_0 C_p \frac{\partial T}{\partial t} = \chi \boldsymbol{\tau} : \mathbf{D}^{vp} \quad (24)$$

By doing so, the coupled thermo-elasto-viscoplastic problem is reduced to a mechanical problem. Eq. (5) suffices as the Galerkin weak formulation of the problem, and the energy equation (24) is only used in the constitutive update.

A rate form constitutive equation is used

$$\overset{\triangledown}{\boldsymbol{\tau}} := \mathbf{C}^{elas} \Big(\mathbf{D} - \mathbf{D}^{vp} - \mathbf{D}^T \Big), \quad (25)$$

where the Jaumann rate of Kirchhoff stress, $\overset{\triangledown}{\boldsymbol{\tau}}$, is defined as

$$\overset{\triangledown}{\boldsymbol{\tau}} = \dot{\boldsymbol{\tau}} - \mathbf{W}\boldsymbol{\tau} + \boldsymbol{\tau}\mathbf{W} \quad (26)$$

and

$$\mathbf{D} := D_{ij} \mathbf{e}_i \otimes \mathbf{e}_j , \qquad D_{ij} := \frac{1}{2} \Big(\frac{\partial v_i}{\partial x_j} + \frac{\partial v_j}{\partial x_i} \Big) \quad (27)$$

$$\mathbf{W} := W_{ij} \mathbf{e}_i \otimes \mathbf{e}_j , \qquad W_{ij} := \frac{1}{2} \Big(\frac{\partial v_i}{\partial x_j} - \frac{\partial v_j}{\partial x_i} \Big) \quad (28)$$

The yield surface of viscoplastic solid is of von Mises type,

9

$$D_{ij}^{vp} := \bar{\eta}(\bar{\sigma}, \bar{\epsilon}, T)\frac{\partial f}{\partial \sigma_{ij}} \tag{29}$$

$$f(\bar{\sigma}, \kappa) = \bar{\sigma} - \kappa = 0 \tag{30}$$

$$\bar{\sigma}^2 = \frac{3}{2}s_{ij}s_{ij}, \tag{31}$$

$$s_{ij} = \tau'_{ij} - \alpha_{ij} \tag{32}$$

$$\tau'_{ij} = \tau_{ij} - \frac{1}{3}tr(\boldsymbol{\tau})\delta_{ij} \tag{33}$$

$$\bar{\epsilon} := \int_0^t \sqrt{\frac{2}{3}\mathbf{D}^{vp} : \mathbf{D}^{vp}} \; dt \tag{34}$$

A thermo-elasto-viscoplastic material model is adopted (See Zhou et al [33]), which is described as

$$\bar{\eta} = \dot{\epsilon}_0 \Big[\frac{\bar{\sigma}}{g(\bar{\epsilon}, T)}\Big]^m , \tag{35}$$

$$g(\bar{\epsilon}, T) = \sigma_0[1 + \bar{\epsilon}/\epsilon_0]^N \left\{1 - \delta\Big[\exp\Big(\frac{T - T_0}{\kappa}\Big) - 1\Big]\right\} \tag{36}$$

where m is the power index. The thermal rate of deformation, $\mathbf{D}^T$, is given as

$$\mathbf{D}^T = \alpha\dot{T}\mathbf{1} \tag{37}$$

where α is the coefficient of thermal expansion.

3.1 Constitutive Update

The constitutive update follows largely the rate tangent modulus method proposed by Peirce et al. [27], which has been used in the context of thermo-viscoplasticity by LeMond & Needleman [12,11]. The essence of the rate tangent modulus method is to approximate a function of time in the interval $t_{n+\theta} \in [t_n, t_{n+1}]$, $\theta \in [0, 1]$, as

$$f_\theta := (1 - \theta)f_n + \theta f_{n+1} \tag{38}$$

Thus, if we choose the predicted velocity field at t_{n+1} as $\mathbf{v}_{n+1}^{trial} = \mathbf{v}_n + \Delta t \mathbf{a}_n$, then it follows that

$$\mathbf{v}_\theta = (1 - \theta)\mathbf{v}_n + \theta\mathbf{v}_{n+1}^{trial} = \mathbf{v}_n + \theta\Delta t \mathbf{a}_n \tag{39}$$

$$\mathbf{u}_\theta = (1 - \theta)\mathbf{u}_n + \theta\mathbf{u}_{n+1} = \mathbf{u}_n + \Delta t\theta\mathbf{v}_n + \theta^2\Delta t^2\mathbf{a}_n \tag{40}$$

$$\mathbf{L}_\theta = \mathbf{v}_\theta \overleftarrow{\nabla}_\mathbf{x} = \Big(\mathbf{v}_\theta \overleftarrow{\nabla}\mathbf{x}\Big) \cdot \mathbf{F}_{n+1}^{-1} \tag{41}$$

$$\mathbf{D}_\theta = \frac{1}{2}\Big(\mathbf{L}_\theta + \mathbf{L}_\theta^T\Big) \tag{42}$$

$$\mathbf{W}_\theta = \frac{1}{2}\Big(\mathbf{L}_\theta - \mathbf{L}_\theta^T\Big) \tag{43}$$

For $\theta = 1/2$, the predict step, or trial step corresponds to the centeral difference scheme. Hence, the kinematical variables are known at the configuration $t_{n+\theta}$.

The main task here is to update the Kirchhoff stress:

$$\boldsymbol{\tau}_{n+1} = \boldsymbol{\tau}_n + \dot{\boldsymbol{\tau}}_\theta \Delta t \tag{44}$$

$$\dot{\boldsymbol{\tau}}_\theta \approx \overset{\triangledown}{\boldsymbol{\tau}}_\theta + \mathbf{W}_\theta \cdot \boldsymbol{\tau}_n + \boldsymbol{\tau}_n \cdot \mathbf{W}_\theta^T \tag{45}$$

To accomplish this, one has to first find $\dot{\bar{\epsilon}}_\theta$, and then $\overset{\triangledown}{\boldsymbol{\tau}}_\theta$. Let

$$\dot{\bar{\epsilon}}_\theta = (1 - \theta)\dot{\bar{\epsilon}}_n + \theta\dot{\bar{\epsilon}}_{n+1} \tag{46}$$

where $\dot{\bar{\epsilon}}_{n+1}$ is approximated by a first order Taylor series expansion in $\bar{\sigma}, \bar{\epsilon}$ and T,

$$\dot{\bar{\epsilon}}_{n+1} = \dot{\bar{\epsilon}}_n + \Delta t\Big[\frac{\partial \dot{\bar{\epsilon}}}{\partial \bar{\sigma}}\Big|_n \dot{\bar{\sigma}}_\theta + \frac{\partial \dot{\bar{\epsilon}}}{\partial \bar{\epsilon}}\Big|_n \dot{\bar{\epsilon}}_\theta + \frac{\partial \dot{\bar{\epsilon}}}{\partial T}\Big|_n \dot{T}_\theta\Big] \tag{47}$$

Let

$$\mathbf{p} := \frac{3}{2}\frac{s'}{\bar{\sigma}} \tag{48}$$

The same procedure may be applied to other state variables as well,

$$\mathbf{d}_\theta^{vp} = \dot{\bar{\epsilon}}_\theta \mathbf{p}_n \tag{49}$$

$$\overset{\triangledown}{\boldsymbol{\alpha}}_\theta = b\mathbf{d}_\theta^{vp} \tag{50}$$

$$\dot{\boldsymbol{\alpha}}_\theta = \overset{\triangledown}{\boldsymbol{\alpha}}_\theta + \mathbf{W}_\theta \cdot \boldsymbol{\alpha}_n + \boldsymbol{\alpha}_n \cdot \mathbf{W}_\theta^T \tag{51}$$

$$\boldsymbol{\alpha}_{n+1} = \boldsymbol{\alpha}_n + \dot{\boldsymbol{\alpha}}_\theta \Delta t \tag{52}$$

Since $\mathbf{p}_\theta$ and $\boldsymbol{\alpha}_\theta$ are unknown, inconsistent approximations are taken $\mathbf{p}_\theta \approx \mathbf{p}_n$ $\boldsymbol{\alpha}_\theta \approx \boldsymbol{\alpha}_n$ in the explicit calculation, which shall be elaborated further.

In isotropic hardening

$$\mathbf{D}^{vp} = \frac{3}{2}\frac{\dot{\bar{\epsilon}}}{\bar{\sigma}}\boldsymbol{\tau}' \tag{53}$$

11

hence

$$\boldsymbol{\tau} : \mathbf{D}^p = \left(\boldsymbol{\tau}' + \frac{1}{3}tr(\boldsymbol{\tau})\mathbf{1}\right) : \left(\frac{3}{2}\frac{\dot{\bar{\epsilon}}}{\bar{\sigma}}\boldsymbol{\tau}'\right) = \frac{3}{2}\frac{\dot{\bar{\epsilon}}}{\bar{\sigma}}\boldsymbol{\tau}' : \boldsymbol{\tau}' = \bar{\sigma}\dot{\bar{\epsilon}} \qquad (54)$$

Eq. (24) can rewritten as

$$\frac{\partial T}{\partial t} = \frac{\chi}{\rho_0 C_p}\bar{\sigma}\dot{\bar{\epsilon}} \qquad (55)$$

Utilizing (55), we propose the following *monolithic* or *simultaneous* rate tangent modulus scheme. Let

$$\dot{T}_\theta = \frac{\chi\bar{\sigma}_\theta}{\rho_0 C_p}\dot{\bar{\epsilon}}_\theta \qquad (56)$$

Substituting (56) into (47), we have

$$\dot{\bar{\epsilon}}_{n+1} = \dot{\bar{\epsilon}}_n + \Delta t_n\left\{\frac{\partial\dot{\bar{\epsilon}}}{\partial\bar{\sigma}}\Big|_n\dot{\bar{\sigma}}_\theta + \frac{\partial\dot{\bar{\epsilon}}}{\partial\bar{\epsilon}}\Big|_n\dot{\bar{\epsilon}}_\theta + \frac{\partial\dot{\bar{\epsilon}}}{\partial T}\Big|_n\left(\frac{\chi}{\rho_0 C_p}\bar{\sigma}_\theta\dot{\bar{\epsilon}}_\theta\right)\right\} \qquad (57)$$

Then substituting (57) into (46) and solving for $\dot{\bar{\epsilon}}_\theta$ yields

$$\dot{\bar{\epsilon}}_\theta = \frac{\dot{\bar{\epsilon}}_n}{1 + \xi_\theta} + \frac{1}{H_\theta}\frac{\xi_\theta}{1 + \xi_\theta}\mathbf{P}_\theta : \mathbf{D}_\theta \qquad (58)$$

where

$$H_\theta := \frac{3E}{2(1 + \nu)} - \frac{\partial\dot{\bar{\epsilon}}/\partial\bar{\epsilon}}{\partial\dot{\bar{\epsilon}}/\partial\bar{\sigma}}\Big|_n - \frac{\partial\dot{\bar{\epsilon}}/\partial T}{\partial\dot{\bar{\epsilon}}/\partial\bar{\sigma}}\Big|_n\frac{\alpha\chi}{\rho_0 C_p}\bar{\sigma}_\theta$$

$$\approx \frac{3E}{2(1 + \nu)} - \frac{\partial\dot{\bar{\epsilon}}/\partial\bar{\epsilon}}{\partial\dot{\bar{\epsilon}}/\partial\bar{\sigma}}\Big|_n - \frac{\partial\dot{\bar{\epsilon}}/\partial T}{\partial\dot{\bar{\epsilon}}/\partial\bar{\sigma}}\Big|_n\frac{\alpha\chi}{\rho_0 C_p}\bar{\sigma}_n \qquad (59)$$

$$\mathbf{P}_\theta := \mathbf{C}^{elas} : \mathbf{p}_\theta \approx \mathbf{C}^{elas} : \mathbf{p}_n \qquad (60)$$

$$\xi_\theta = \theta\Delta t\left(\frac{\partial\dot{\bar{\epsilon}}}{\partial\bar{\sigma}}\right)_n H_\theta \qquad (61)$$

Note that since we don't know the stress state at the configuration $\Omega_{n+\theta}$, in an explicit update procedure we approximate σ_θ by σ_n in the calculations of H_θ, $\mathbf{P}_\theta$, as well as ξ_θ. This assumption might be implied in the original derivation of Peirce [27], nonetheless it never made clear explicitly.

By simple calculation, one will have

$$\frac{\partial \dot{\bar{\epsilon}}}{\partial \bar{\sigma}} = \frac{m\dot{\bar{\epsilon}}}{\bar{\sigma}} \tag{62}$$

$$\frac{\partial \dot{\bar{\epsilon}}/\partial T}{\partial \dot{\bar{\epsilon}}/\partial \bar{\sigma}} = -\left(\frac{\bar{\sigma}}{g}\right)\frac{\partial g}{\partial T} \tag{63}$$

$$\frac{\partial \dot{\bar{\epsilon}}/\partial \bar{\epsilon}}{\partial \dot{\bar{\epsilon}}/\partial \bar{\sigma}} = -\left(\frac{\bar{\sigma}}{g}\right)\frac{\partial g}{\partial \bar{\epsilon}} \tag{64}$$

Subsequently, the Jaumann rate of the Kirchhoff stress is evaluated as

$$\overset{\triangledown}{\mathcal{T}}_\theta = \mathbf{C}_\theta^{tan} : \mathbf{D}_\theta - \left\{\frac{\dot{\bar{\epsilon}}_n}{1+\xi_\theta}\right\}\left[\mathbf{P}_\theta + 3K\alpha\frac{\chi\bar{\sigma}_\theta}{\rho C_p}\mathbf{1}\right] \tag{65}$$

where

$$\mathbf{C}_\theta^{tan} = \mathbf{C}^{elas} - \frac{\xi_\theta}{H_\theta(1+\xi_\theta)}\left[\mathbf{P}_\theta \otimes \mathbf{P}_\theta + (3\lambda + 2\mu)\alpha\frac{\chi\bar{\sigma}_n}{\rho_0 C_p}\mathbf{1} \otimes \mathbf{P}_\theta\right] \tag{66}$$

is the adiabatic tangent stiffness, which is not symmetric. Assuming that $\bar{\epsilon}_\theta$ and $\bar{\sigma}_\theta$ are available after the stress update, the temperature can then be updated at each quadrature point as

$$T_{n+1} = T_n + \dot{T}_\theta \Delta t \tag{67}$$

where

$$\dot{T}_\theta = \frac{\chi}{\rho_0 C_p}\dot{\bar{\epsilon}}_\theta \bar{\sigma}_\theta \tag{68}$$

It seems to authors that the above adiabatic rate tangent modulus method has not been published in literature.

3.2 Modeling Fracture and Shear Band

To simulate fracture and crack growth, a simple material damage (erosion) algorithm is implemented, which is controlled by a maximum tensile stress criterion. The algorithm works as follows: when the maximum tensile stress at a material point exceeds a certain limit, we declare that the crack is passing through that material point, and to approximate the cracking, or fracture process, we reset the stress components at that material point to zero, the value of temperature to room temperature, i.e. we basically take out that material point from the computation. By doing this, some conservation properties of specimen may be lost, because implicitly the mass is not conserved anymore,

13

and so are the other quantities. However, since there are only small portion of material being eroded (say less than 0.1 %), the accuracy of the algorithm is reasonably good in computations.

In most of numerical simulations of strain localization, shear band formation is the outcome of a bifurcated solution sought in numerical computations due to material instability. However, how to simulate the propagation of such material instability is still an open problem at large, and as mentioned in the beginning, most of previous numerical simulations fail in simulating the propagation of shear band formation. **The key technical ingradient in such simulations, we believe, is how to simulate the collapsing state of shear band formation. And it is found that the stress collapse in the newly formed localization zone (shear band tip) promotes or triggers the shear band's further propagating.** To simulate stress collapse state inside the shear band, a so-called shear band damage model is introduced, which conforms physicist's belief that instead of being a bifurcated mathematical solution shear band is a physical entity, within which there are significant weakening, or changes in material properties, and it may even be identified as phase transformation (See Giovanola [7,8]). In this paper, to simulate the collapsing state of shear band formation, a thermal-viscous Newtonian fluid damage model proposed by Zhou et al [33] is used, which can describe the drastic reduction of shear strength in shear band region. To justify employing such multi-physics model, a detailed discussion shall be carried out in the Part II of this work, and the model used here (i.e. Zhou-Rosakis model) is made in comparison with an earlier model by Freund & Hutchinson [4], which was used in an analysis of dynamic fracture under high strain rate condition.

1. *Cleavage Failure* The main advantages of using this simple material damage algorithm is its simplicity. By doing so, one can simulate crack growth without remeshing, which may save a lot of memory for book-keeping, and CPU time for solving complex algebraic equations to determine crack's incremental orientation, as well as update connectivity array (in finite element calculation). Since the nonlocal nature of meshfree interpolation, the connectivity relation with respect to referential configuration among particles and quadrature points do need being updated to prevent the particles in the other side of the crack have interpolating contribution over the crack line. A less accurate, but efficient way to get around connectivity updating is that once in a background cell there is one quadrature point is damaged, we then declare that all the other quadrature points in the same background cell are damaged as well. The consequence of this approximation is more material points being eroded, and the crack has a finite width (that is why it may prevent the crossover interpolation).

Since the specimen is thin (6 *mm*), the crack morphology observed in the experiment is always uniform in the thickness direction. Therefore, it may

be reasonable to assume that the cleavage fracture toughness in the thermo-elasto-viscoplastic solid is controlled by the maximum circumferential stress, or hoop stress within the plane, which conforms with the conventional theory in brittle fracture (e.g. Erdogan & Sih [3]). In our numerical computation, the following criterion is used

$$\sigma_{max} \geq \sigma_{cr} \tag{69}$$

where the critical stress is set as $\sigma_{cr} = 3\sigma_0$ (where σ_0 is the initial yield stress). When maximum principle stress reaches $3\sigma_0$ at a material point (Gauss quadrature point), we set

$$\tau_{ij} = 0 \ ; \quad D_{ij} = 0 \ ; \quad T = T_0 \ , \tag{70}$$

2. *Shear Band Damage*

How to simulate the shear band propagation is still an open subject. This is a question that is related why shear band can propagates. Initially, there is a naive notion among some researchers that analogous to crack propagation, there may be a stress concentration region in front of the tip of strain localization zone, and as external loading continues, the material instability can proceed automatically in successive fashion. However, as have been shown by Gioia and Ortiz [6], the stress field near the initial strain localization zone at the pre-notch tip in a thermo-elastic-viscoplastic material, is somewhat diffusive towards the shear band tip, which has been confirmed by the numerical analysis done by Needleman [25] for for elasto-viscoplastic material. This genetic "diffusive" stress field in front of the "tip" of strain localization zone prevent material instability to advance in a successive, or catastrophic successive manner. On the other hand, experimental results strongly indicate a phenomenon of successive/automatic advancement of strain localization zone, i.e., dynamic shear band propagation. This implies that dynamic shear band propagation is controlled by the intensity of some other physical quantities other than stress field.

The only analytical condition available that may be related to the stress collapse is the localization condition of Molinari and Clifton [22]. Gioia and Ortiz showed [6] that when Molinari-Clifton condition is met, steady adiabatic boundary layer collapse into a vortex sheet. Nevertheless, how to efficiently implement Molinari-Clifton condition in the case of dynamic shear band propagation is still an open problem. It have been speculated for a long time that that there is an intensified high strain rate zone at the shear band tip [31,30,32] in the case of high strain rate loading. Moreover, the micrograph of shear band surface indicates that there is uniform void distribution throughout the shear band damage zone [34]. It is suggested that dynamic shear band propaga-

15

tion may be a damage evolution process, which is controlled by strain rate. We believe that it is highly plausible that the magnitude of strain rate could be a critical measurement of shear band toughness [6], and it is possible that once the strain rate reaches a certain level, shear band damage occurs irreversibly, and the material changes its behaviors inside the shear band damage zone, and consequently material loss its shear stress carrying capability significantly. The underline argument here is dynamic shear band propagation is a type of damage evolution process, though a systematic theory is needed, and it is still missing !

Following Zhou et al. [33], the ductile failure condition is controlled by the strain rate

$$\bar{\epsilon}_{cr} = \epsilon_1 + (\epsilon_2 - \epsilon_1)\frac{\dot{\epsilon}_r}{(\dot{\epsilon}_r + \dot{\bar{\epsilon}})} \tag{71}$$

where ϵ_1, ϵ_2 and $\dot{\epsilon}_r$ are given parameters. After $\bar{\epsilon}$ reaches $\bar{\epsilon}_{cr}$, the damaged material is assumed to no longer have shear-stress carrying capacity, and it behaviors like a Newtonian viscous fluid,

$$\boldsymbol{\tau} = \frac{\gamma[1 - J + \alpha(T - T_0)]}{J}\frac{E}{1 - \nu}\mathbf{1} + \mu\mathbf{D} \tag{72}$$

where γ is the stiffness parameter, and μ is the viscosity.

4 Numerical Results

4.1 Opening discussion

The computations carried out in this work is mainly based on the experiments conducted by Rosakis and his co-workers at California Institute of Technology, i.e. the so-called Zhou-Rosakis-Ravichandran problem. The experiment is an impact test between a single pre-notch plate and a cylinder projectile as shown in Fig. 3. In this numerical study, two computational configurations have been used to simulate the specimens with different sizes, which are corresponding to the two different sets of experiment. The first one is used in the experiment by Zhou, Rosakis, and Ravichandran [34] (see Fig. 4 (a)), the second one is used by Pradeep, Rosakis, and Ravichandran [28] (see Fig. 4 (b)). It may be noted that in the second specimen, there is a $2mm$ long fatigue crack in front of pre-notch, which increases the acuity of the original pre-notched crack.

---

[6] the authors here are inclined to discard the notion of using dynamic J-integral as the measurement of the shear band toughness.

16

pages 17 to 20

When impact velocity exceeds certain limit[7], the cleavage crack mode is suppressed, there is shear band that is initiated from the crack tip, and propagates through the specimen. Since the impact is due to an unsymmetric collision between the bullet and plate, the shear band propagates slightly towards the lower part of the specimen, rather than penetrating through the specimen parallel with horizontal line, the orientation of pre-notched crack.

By comparing it with the results in mediate range impact, one will observe a mode failure transition, i.e. from the cleavage type of failure at lower impact speed to the ductile failure at high impact speed. Meshfree simulations are accurately validated such failure mode transition.

A sequence of 3D calculations have been displayed in Figure (8) and (9), which describe the evolution process of shear band propagation. (10)

As reported by Zhou et al (1996a), the experimental results indicates that the shear band formation is a curved surface. Such shear band morphology is very difficult to be captured in finite element based simulation, because of the mesh alignment sensitivity that is inherent in finite element simulations. Using meshfree methods, such curve shearband formation has been recaptured in numerical computations.

A 2D view of 3D computations is shown in Figure (10); temperature profiles are displayed, which is main characterizations of shear band formation.

In 3D computation, a "temperature reflection" phenomenon has been observed. That is before the shear band tip reaches to the lateral surface of the specimen, the temperature at intersection point of arriving shear band path and the lateral surface has already rised first, which is similar to the spalling phenomenon of target/projectile problem, i.e. before the projectile penetrates the target, fragmentation has already occurred at exit surface. A plausible explanation for such temperature reflection is that a possible plastic wave has reached the lateral surface first before shear band's arriving, and the free-surface condition amplifies that plastic wave loading, and cause temperature rising. It should be noted that this phenomenon has been only observed in 3D simulation, and it is the only significant 3D effect that has been observed in our meshfree computations (see Figure 7).

From Figure (10), one may see that the shear band formation computed by meshfree method is slightly curved towards the lower half of the specimen,

---

[7] In the experiments conducted by Zhou et al (1996a), this critical velocity is 29.6 m/s for C-300 steel with the specific size, geometry of the specimen.

pages 22 to 26

to severe material strength weakening. Thus, they proposed so-called Newtonian fluid damage model to represent shear band's low shear-stress carrying capability. We believe that the so-called damage state of the shear band is the stress collapse state that Wright has referred to [31]. Thus, it is justifiable to use quasi-fluid model, or purely visco-plastic flow model to mimic damaged shear band.

It has been found in this numerical simulation that there is autonomous high strain rate region ahead of the shear band tip. Such autonomous region is locally self-similar in shape, and has very high strain rate concentration, which carries and controls the growth and propagation of the adiabatic shear band (See Fig. 13). It is our opinion that this autonomous, self-similar, high strain rate concentration, local field in front of the propagation shear band tip plays a similar role as the autonomous singular stress field at a propagating crack tip in elastodynamic fracture mechanics, and once the strain rate reaches a threshold, the stress state in the newly formed localization zone collapse.

Other self-similar, local state variable fields have also been observed, such as there is a local delta region of σ_{11} in front of shear band tip , and there is also a low value shear stress, σ_{12}, basin moving with the shear band tip, which have been reported by the finite element simulation conducted by Zhou et al [33].

The last issue is the shear band length/speed history after the impact. By comparing to the experiments conducted by Zhou et al [34], the general trend of both shear band length histories, as well as shear band velocities histories follow the experiment results. For instance, at high speed impact, within $60m/s$, shear band penetrates the specimen. However, based on the numerical computation at $V_0 = 35m/s$, the highest shear band speed is up to $2000m/s$, up to 60% of the shear wave speed, which has not yet been reported in experimental observations. In experiments, the shear band speed is only up to $1200m/s$, at 38% of the shear wave speed. On the other hand, the measurement depends on the definition of a shear band, i.e. what defines a shear band ? In the measurement of shear length, as well as shear band speed, the current study adopts two definitions. One of them is choosing the the effective strain criterion, that is we choose effective strain at 12.5% mark as the threshold of a shear band; another practical criterion is choosing the temperature rising (for adiabatic shear band only) above $50^o K$ mark from room temperature, or $50^o K$ mark above ambient temperature as the threshold of shear band. Figure (15) is produced based on the second criterion.
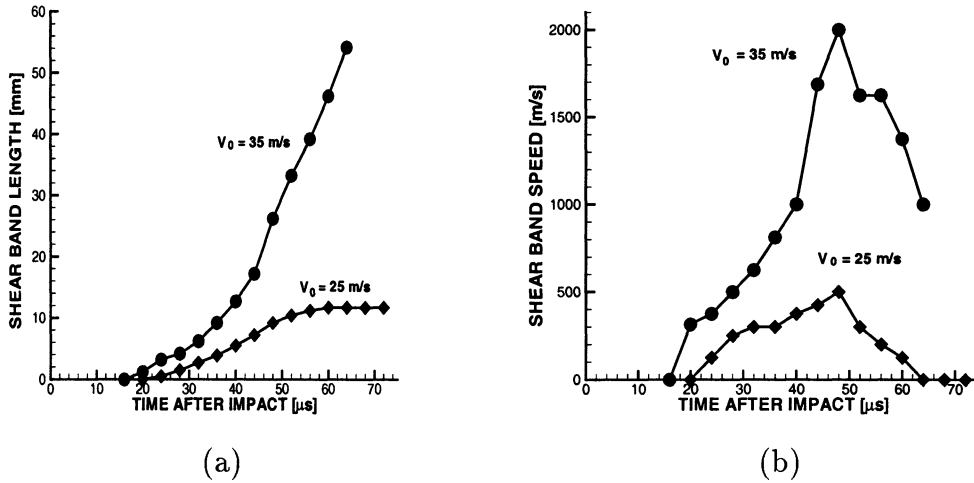
pages 28 to 29

Fig. 15. (a) Shear band length histories at different impact velocities; (b) Shear band speed histories at different impact velocities

5 Concluding Remarks

In this work, a meshfree discretization/approximation has been used in a simple explicit displacement based formulation to simulate dynamic shear propagation in a pre-notch plate with impact loading.

The main contributions of this study are: (1) the numerical computation reported here have successfully simulated the failure mode transition/switch that have been observed in the experiments, and have not been able to simulate in previous numerical computations. (2) the numerical simulation confirms that there is a self-similar, autonomous state variable field moving with shear band tip, as much like as the self-similar, singular stress filed in front of the tip of a propagating, brittle crack in elastodynamics. Among which, the strain rate distribution is concentrated in front of running shear band tip, which is speculated as the primary factor to drive the shear band, or to the shear band growth. (3) The key to simulate the dynamic shear band propagation is to assume that adiabatic shear band can propagates only if the newly-formed localization zone suffers a stress collapse. And we tend to believe that the strain rate concentration triggers the stress collapse just as the stress concentration triggers the material fracture.

In addition, we have found that there is crack formed along the interface between the shear band and matrix without introducing any damage model that accounts for microvoid growth and coalescence. And also there is a "temperature reflection" phenomenon observed in numerical experiment.

30

Acknowledgement

References

[1] T. Belytschko, Y. Y. Lu, and L. Gu. Element free galerkin methods. *International Journal for Numerical Methods in Engineering*, 37:229–256, 1994.

[2] T. Belytschko and M. Tabbara. Dynamic fracture using element-free galerkin methods. *International Journal for Numerical Methods in Engineering*, 39:3–48, 1996.

[3] F. Erdogan and G. C. Sih. On the crack extension in plates under plane loading and transverse shear. *Journal of Basic Engineering*, 85D:519–527, 1963.

[4] L. B. Freund and J. W. Hutchinson. High strain-rate crack growth in rate-dependent plastic solids. *Journal of Mechanics and Physics in Solids*, 33:169–191, 1985.

[5] H. Gao and P. Klein. Numerical simulation of crack growth in an isotropic solid with randomized internal cohesive bonds. *Journal of Mechanics and Physics of Solids*, 46:187–218, 1999.

[6] G. Gioia and M. Ortiz. The two-dimensional structure of dynamic boundary layers and shear bands in thermoviscoplastic solids. *Journal of Mechanics and Physics of Solids*, 44:251–291, 1996.

[7] J. Giovanola. Adiabatic shear banding under pure shear loading. 1. direct observation of strain localization and energy measurements. *Mechanics of Materials*, 7:59–71, 1988.

[8] J. Giovanola. Adiabatic shear banding under pure shear loading. 2. fractographic and metallographic observations. *Mechanics of Materials*, 7:72–87, 1988.

[9] J. F. Kalthoff. Shadow optical analysis of dynamic shear fracture. *SPIE, Photomechanics and Speckle Metrology*, 814:531–538, 1987.

[10] P. A. Klein. Simulations of the kalthoff-winkler experiment. Technical report, Tech. Report, Sandia National Laboratories, 1999.

[11] J. LeMonds and A. Needleman. An analysis of shear band development incorporating heat conduction. *Mechanics of Materials*, 5:363, 1986.

[12] J. LeMonds and A. Needleman. Finite element analysis of shear localization in rate and temperature dependent solids. *Mechanics of Materials*, 5:339–361, 1986.

[13] S. Li, W. Hao, and W. K. Liu. Meshfree simulations shear banding under large deformation. *International Journal of Sloids and Structures*, 2000.

[14] S. Li and W. K. Liu. Reproducing kernel hierarchical partition of unity part i: Formulation & theory. *International Journal for Numerical Methods in Engineering*, 45:251–288, 1999.

[15] S. Li and W. K. Liu. Numerical simulations of strain localization in inelastic solids using meshfree methods. *International Journal of Numerical Methods for Engineering*, 48:1285–1309, 2000.

[16] W. K. Liu, Y. Chen, R. A. Uras, and C. T. Chang. Generalized multiple scale reproducing kernel particle methods. *Computer Methods in Applied Mechanics and Engineering*, 139:91–158, 1996.

[17] W. K. Liu, S. Jun, S. Li, J. Adee, and T. Belytschko. Reproducing kernel particle methods for structural dynamics. *International Journal for Numerical Methods in Engineering*, 38:1655–1679, 1995.

[18] W. K. Liu, S. Jun, and S. Zhang. Reproducing kernel particle methods. *International Journal of Numerical Methods in Fluids*, 20:1081–1106, 1995.

[19] W. K. Liu, S. Li, and T. Belytschko. Moving least square reproducing kernel method part i: Methodology and convergence. *Computer Methods in Applied Mechanics and Engineering*, 143:422–433, 1997.

[20] W. K. Liu, R. A. Uras, and Y. Chen. Enrichment of the finite element method with reproducing kernel particle method. *ASME Journal of Applied Mechanics*, 64:861–870, 1997.

[21] J. J. Mason, A. J. Rosakis, and G. Ravichandran. Full field measurement of the dynamic deformation field around a growing adiabatic shear band at the tip of a dynamically loaded crack or notch. *Journal of Mechanics and Physics of Solids*, 42:1679–1697, 1994.

[22] A. Molinari and R. J. Cliffton. Analytical characterization of shear localization in thermoviscoplastic materials. *ASME Journal of Applied Mechanics*, 54:806–812, 1987.

[23] J. J. Monaghan. An introduction to shp. *Computation Physics Communication*, 48:89–96, 1988.

[24] B. Nayroles, G. Touzot, and P. Villon. Generalizing the finite element method: Diffuse approximation and diffuse elements. *Computational Mechanics*, 10:307–318, 1992.

[25] A. Needleman. Dynamic shear band development in plane strain. *Journal of Applied Mechanics*, 56:1–9, 1989.

[26] A. Needleman and V. Tvergaard. Analysis of a brittle-ductile transition under dynamic shear loading. *International Journal of Solids and Structures*, 32:2571–2590, 1995.

[27] D. Peirce, C. F. Shih, and A. Needleman. A tangent modulus method for rate dependent solids. *Computer & Structure*, 5:875–887, 1984.

[28] A. J. Rosakis, P. Guduru, and G. Ravichandran. Private communication. 2000.

[29] G. I. Taylor and H. Quinney. The latent energy remaining in a metal; after cold working. *Proc. R. Soc. A*, 143:307–326, 1934.

[30] T. W. Wright. Scaling laws for adiabatic shear bands. *International Journal of Solids and Structures*, 32:2745–2750, 1995.

[31] T. W. Wright and J. W. Walter. On stress collapes in adiabatic shear band. *Journal of Mechanics and Physics of Solids*, 35:701–720, 1987.

[32] T. W. Wright and J. W. Walter. The asymptotic structure of an adibatic shear band in antiplane motion. *Journal of Mechanics and Physics of Solids*, 44:77–97, 1996.

[33] M. Zhou, G. Ravichandran, and A. J. Rosakis. Dynamically propagating shear bands in impact-loaded prenotched plates—ii. numerical simulations. *Journal of Mechanics of Physics and Solids*, 44:1007–1032, 1996.

[34] M. Zhou, A. J. Rosakis, and G. Ravichandran. Dynamically propagating shear bands in impact-loaded prenotched plates—i. experimental investigations of temperature signatures and propagation speed. *Journal of Mechanics of Physics and Solids*, 44:981–1006, 1996.

[35] M. Zhou, A. J. Rosakis, and G. Ravichandran. On the growth of shear bands and failure-mode transition in prenotched plates: A comparision of singly and doubly notched specimens. *International Journal of Plasticity*, 14:435–451, 1998.